Planetary remote sensing with physical scattering models

Olli Wilkman

ACADEMIC DISSERTATION

Department of Physics
Faculty of Science
University of Helsinki
Helsinki, Finland

To be presented, with the permission of the Faculty of Science of the University of Helsinki, for public criticism in Physicum E204 on June 2nd 2016.

Helsinki 2016

Cover picture: A simulated regolith medium with packing density 0.15.

Abstract

Understanding the light scattering properties of Solar System bodies is important, especially in the case of the small bodies. For these objects, most of our data is photometric, i.e. measurements of the brightness of light in broad spectral bands in visible and near-infrared. Though limited in many ways, these data can be used to derive physical properties that provide constraints on the structure and material composition of the objects. These atmosphereless bodies are almost always covered with a blanket of loose material called the regolith. The planetary regoliths consist of a range of grain sizes from micrometres to tens of metres, and have a complex geological history and chemical composition.

We study two models for the reflectance of planetary surfaces. One is the Lommel-Seeliger model, which is mathematically simple, but also not truly applicable to particulate media such as regoliths. However, an analytical form exists for the integrated brightness of an ellipsoid with the Lommel-Seeliger scattering model. Ellipsoids are useful as crude shape models for asteroids. Some applications of Lommel-Seeliger ellipsoids are studied in the development of a faster software for the inversion of rotational state and rough shape from sparse asteroid lightcurves.

The other scattering model is a semi-numerical one, developed to model the reflectance of dark particulate surfaces, such as the lunar regolith and the surfaces of many asteroids. The model term representing the shadowing effects in the medium is computed numerically, and is computationally expensive to produce, but after being computed once, it can be saved and reused. The model is applied to disk-resolved photometry of the lunar surface, as well as laboratory measurements of a dark volcanic sand. The lunar surface is the best known extraterrestrial material, while volcanic sands can be used as analogues for basaltic regoliths such as the lunar mare surfaces.

These studies are still early steps in both of the model applications mentioned above. The results show promising avenues for further research. In the case of the Lommel-Seeliger ellipsoids, a statistical inversion scheme is used to gain information

on the spin and shape of sparsely observed asteroids. In the studies with the PM scattering model, it was found to provide good fits to data, and though the interpretation of the model parameters is not clear, they are qualitatively reasonable. Some limitations of the current implementation of the model were found, with clear lines of future improvement. On the whole the model has potential for many applications in disk-resolved photometry of regolith surfaces.

Acknowledgements

I thank my two pre-examiners, professor Heikki Salo of Oulu University and Bernard Schmitt of L'Université Grenoble Alpes, for their comments, as well as my opponent, Dr. Deborah Domingue of the Planetary Science Institute.

I am grateful to my primary supervisor, Karri Muinonen, for his guidance and endless patience. I also thank my secondary advisors Antti Penttilä and Jyri Näränen for insightful conversations and feedback. Of my colleagues in Kumpula, I especially want to thank Jouni Peltoniemi, Grigori Fedorets, and Mikael Granvik, for their contribution to my scientific development.

There are many friends I want to thank for their friendship and good times. All my fellow students over the years in Physicum: Jyri, Antti and Nata, and many others. The other members of the graduate students' IRC channel for peer support. All of my dear friends outside these academic circles, whom I have sadly neglected in the last years. And especially I thank Anne for our friendship and the times we shared during most of this work.

I'm grateful to Leila for the time we've spent together so far, and for putting up with me during this last stressful part of my work.

And finally, I thank my family for always supporting me throughout my life.

List of publications

Paper I: Wilkman, O., Muinonen, K., Videen, G., Josset, J.-L., & Souchon, A. (2014). Lunar photometric modelling with SMART-1/AMIE imaging data. Journal of Quantitative Spectroscopy and Radiative Transfer, 146, 529–539. doi:10.1016/j.jqsrt.2014.01.015T

Paper II: Wilkman, O., Muinonen, K. & Peltoniemi, J. (2015). Photometry of dark atmosphereless planetary bodies: an efficient numerical model. Planetary and Space Science. doi:10.1016/j.pss.2015.06.004

Paper III: Wilkman, O., Gritsevits, M., Zubko, N., Peltoniemi, J. & Muinonen, K. (2016). Photometric modelling for laboratory measurements of dark volcanic ash. Journal of Quantitative Spectroscopy and Radiative Transfer (submitted)

Paper IV: Muinonen, K. O., Wilkman, O. V., Cellino, A., Wang, X. & Wang, Y. (2015). Asteroid lightcurve inversion with Lommel–Seeliger ellipsoids. Planetary and Space Science 118, pp. 227–214.

Paper V: Muinonen, K. O. & Wilkman, O. V. (2016). Spherical albedo of a Lommel-Seeliger scattering ellipsoidal asteroid, Proceedings of the International Astronomical Union, Symposium S318, Asteroids: New Observations, New Models. Chesley, S., Morbidelli, A. & Jedicke, R. (ed.). Cambridge University Press

List of abbreviations

AMIE The Advanced Moon micro-Imager Experiment

BRDF Bidirectional Reflectance Distribution Function

ESA European Space Agency

fBm fractional Brownian motion

FGI Finnish Geospatial Research Institute (formerly the Finnish Geodetic Institute)

FIGIFIGO Finnish Geodetic Institute Field Goniometer

L-S Lommel-Seeliger (also **LS** in subscripts)

MCMC Markov-Chain Monte Carlo

NIR Near-infrared

PM Particulate Medium

SMART-1 Small Missions for Advanced Research in Technology

Contents

1 Introduction

Our Solar System consists of the Sun, eight planets and their moons, as well as a large number of smaller bodies ranging in size from over a thousand kilometres (the dwarf planets) to well under a millimetre (interplanetary dust). The term "small bodies" generally covers the asteroids and comets. The classification of small bodies is somewhat loose, and the differences, e.g., between an asteroid and a dormant comet, or the smallest asteroids and largest meteoroids, are not always clearly drawn. The smaller moons of most planets also resemble asteroids, and indeed many of them are likely to be captured asteroids.

Everything in the Solar System is made of the matter from the interstellar cloud which collapsed over four billion years ago to form the Sun. In the debris disc around the protostar, the material condensed to form larger agglomerations, eventually leading to planetesimals and finally the planets themselves. During their formation and later history, the planets have undergone significant melting, differentiation, and other geological alteration. Compared to them, the small bodies are relatively unaltered, and are thought to be the best preserved representatives of the material in the early Solar System. This is one of the most fundamental motivations for studying the physical and geological properties of asteroids.

There are over 500 000 known asteroids, and more are discovered every day. Figure 1.1 shows the two major populations of asteroids in the Solar System. Approximately half of the asteroid population resides in the *main belt*, a region of space between the orbits of Mars and Jupiter. The second largest group is the Trojan asteroids, which are located along the orbit of Jupiter, rotating with it around the two co-orbital Lagrange points. Figure 1.2 shows a selection of asteroids which have been observed with high-resolution cameras on spacecraft. The largest bodies Ceres and Vesta are roughly spherical in shape, due to their mass, but most asteroids have complex shapes, produced through the fragmentation of larger bodies and subsequent sculpting by impacts.

The *Near-Earth asteroids* have orbits which bring them closer to the Earth. This population is formed from main-belt objects whose orbits are altered by the gravita-
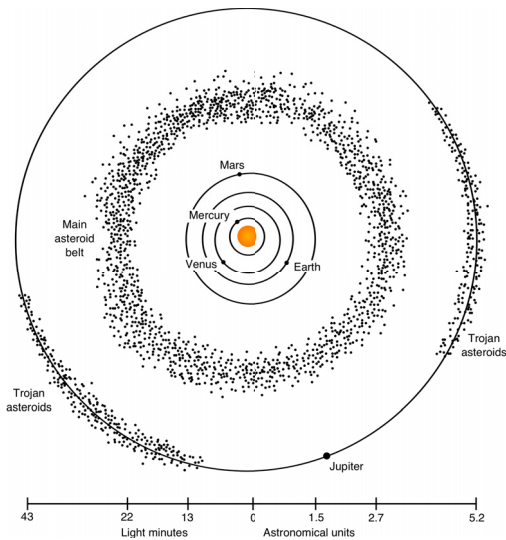
Figure 1.1: A sketch of the largest components of the asteroid population in the Solar System. Image credit: Wikimedia Commons

tional effects of Jupiter, Saturn, and Mars. Some of these asteroids cross the orbit of the Earth and may cause an impact hazard. Characterization of the sizes and physical properties of these potential impactors is needed when considering mitigation strategies. Recently, certain private companies have also been seriously considering near-Earth asteroids as a target for resource exploitation. The asteroids are abundant in many heavier elements which are rare on the Earth. For future large-scale space exploration, resource extraction *in situ* is important, since the cost to lift materials into orbit from the Earth is very high.

1.1 Regolith

The term *regolith* was coined by Merrill (1897) for the "entire mantle of unconsolidated material" covering the bedrock on the Earth. He further described it as "an incoherent mass of varying thickness composed of materials essentially the same as those which make up the rocks themselves, but in greatly varying conditions of mechanical aggregation".

The same definition has since then been extended to the blanket of loose mate-
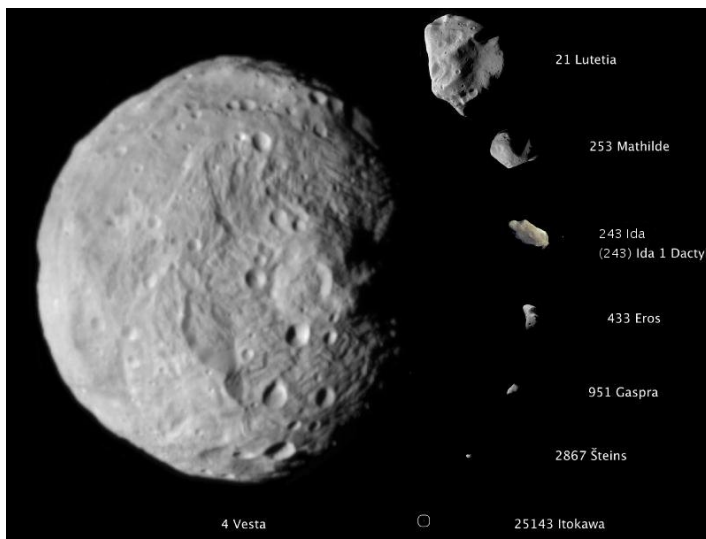
Figure 1.2: A selection of asteroids for which high-resolution images exist. Their sizes are presented in the same scale. The diameter of Vesta is 525 kilometres. Ceres is omitted due to its large size. Together, Ceres and Vesta contain almost 40% of the mass of the entire main belt. Image credit: Wikimedia Commons
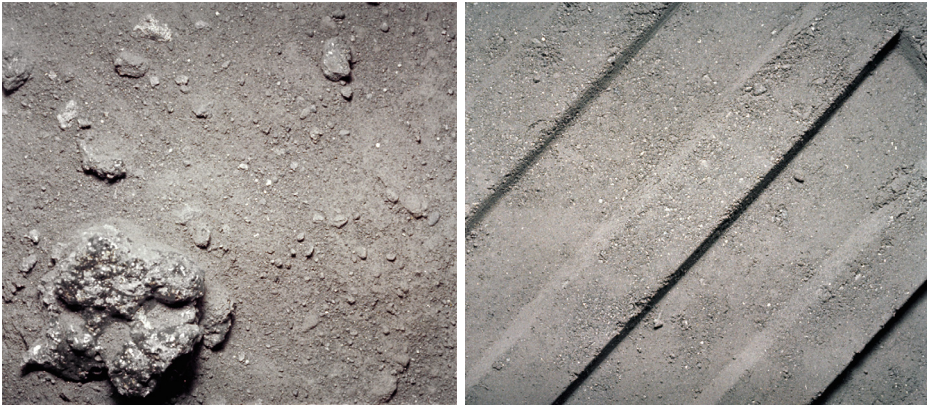
Figure 1.3: Close-ups of the lunar regolith taken with the Apollo Lunar Surface Close-up Camera during the Apollo 12 mission. On the left, relatively undisturbed regolith, and on the right, compressed in an astronaut's footprint. Both images show a patch of surface approximately 7 cm wide. Image credits: NASA.

rial covering the surfaces of Solar System bodies. Practically all bodies in the Solar System are covered by a layer or regolith, produced through the breakup of larger rocks. On the atmosphereless bodies, regolith production is a combination of meteorite impacts, micrometeorite bombardment and thermal stress. The size of the rock fragments increases with depth, and the larger fragments above the bedrock, especially on the Moon, are sometimes called "megaregolith". Many asteroids are believed to have a "rubble-pile" structure, with no significant monolithic component inside. These bodies are, in a way, (mega)regolith all the way down.

Almost all of our remote sensing observations of these bodies are in fact observations of their regolith surfaces. The exceptions are certain high-energy observations such as neutron flux and gamma rays, and longer radar wavelengths which can penetrate through a thin regolith layer. Understanding the properties of the regolith are therefore important in determining the properties of the whole body.

The properties of a regolith include the size and shape distributions of the individual grains, their optical and thermal properties and the way they are packed. Additionally, they can be characterized in terms of the mineralogy and chemical composition. The exact physical properties of a regolith depend on its history and the properties of the parent body.

The chemical composition of regoliths is based on their parent rock, with a minor
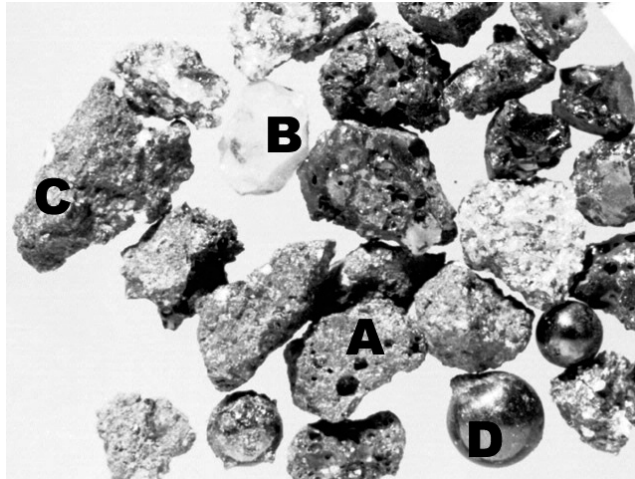
Figure 1.4: Typical lunar mare regolith particles. Grain A is basalt, grain B anorthosite, C is basaltic breccia and D is impact melted glass. The glass spherule D is approximately 1 mm in diameter. (Image credit: NASA photo S70-55663)

contribution from other bodies which have impacted the parent. The topmost layer of the surface is affected by *space weathering*, a general name for the processes that affect materials exposed in space: micrometeorite bombardment, interaction with energetic solar wind particles, and high-energy cosmic rays. Space weathering causes the chemical and physical properties of the exposed minerals to change slowly (Clark, 2002; Gaffey, 2010). This is especially visible in the optical properties. Weathered regolith becomes darker, its reflection spectrum "reddens" (the darkening is faster at the blue end of the visible spectrum) and absorption bands from its mineral composition become less pronounced. Though the weathering only happens in the top nanometres or micrometres of the surface, larger meteorite impacts and seismic processes slowly mix the weathered material with the layers underneath. At the same time fresh regolith is revealed, causing the bright rings and rays around fresh impact craters.

All of the properties of the regolith vary greatly depending on the parent body. The best understood example is the lunar regolith (Figure 1.3), which was studied *in situ* and sampled by astronauts during the Apollo missions (McKay et al., 1991). The lunar regolith has been processed for billions of years and is fine and powder-like on the surface. The regolith layer is up to tens of metres deep in some locations.
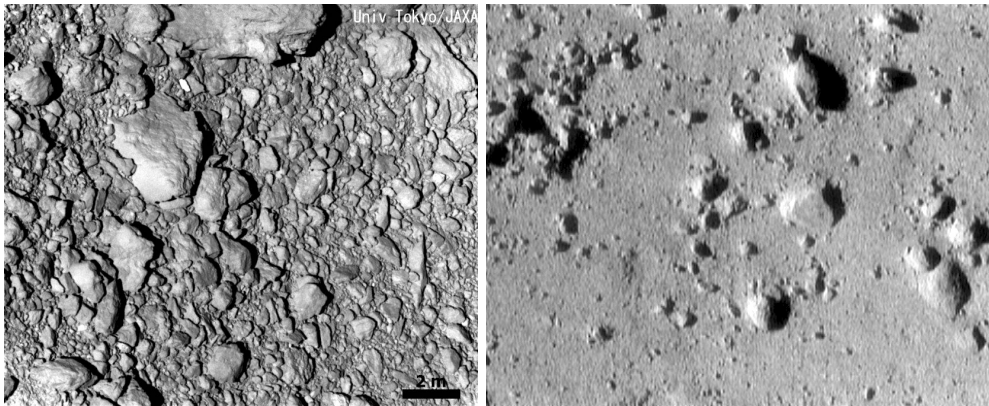
Figure 1.5: Photographs of the regoliths on the asteroids (25143) Itokawa and (433) Eros, both showing a roughly ten metres wide surface patch. This area on Itokawa is covered in rocks and boulders and devoid of fine regolith, while on Eros the fine regolith is filling the gaps between larger fragments. Image credits: University of Tokyo/JAXA and NASA.

Although also containing larger rocks, most of the mass of the top layer is in submillimetre grains. The composition of the regolith is complex, with grains of minerals from many different locations mixed, agglutinated and altered by impacts. Figure 1.4 shows a selection of mare regolith particles.

Asteroid surfaces can have strikingly different appearances (Figure 1.5), even in different parts of the same asteroid. The surface of (433) Eros has large smooth areas with very fine regolith (Veverka et al., 2000), while that of (25143) Itokawa has regions where the fine regolith is almost completely absent and the surface is dominated by rocks and boulders from the centimetre scale upwards (Michikami et al., 2008).

Aside from the lunar material, the only samples of extraterrestrial rocks we have are a few grains of asteroid regolith from Itokawa (Tsuchiyama et al., 2011), returned by the Japanese Hayabusa spacecraft (Figure 1.6), and the collection of meteorites found on the Earth. Most meteorites are pieces of asteroids, ejected by impacts. Some of them come from the Moon or Mars, as a result of large impacts on the surface. The connections between individual meteorites and their parent bodies are difficult to make (Burbine et al., 2002).

Various terrestrial materials can be used as analogs for planetary regoliths (Närä-
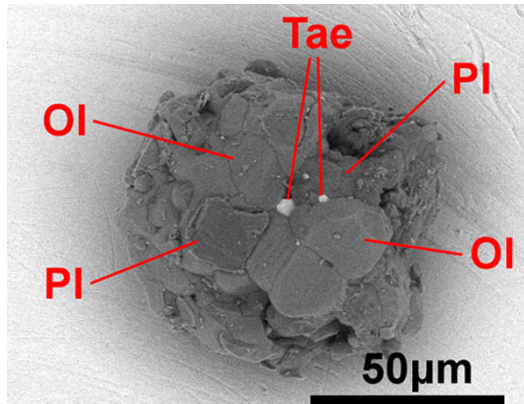
Figure 1.6: Scanning electron microscope image of a dust particle retrieved from the asteroid Itokawa by the Hayabusa mission. The highlighted minerals are olivine, plagioclase, and taenite. The majority of particles retrieved by Hayabusa contained only one mineral, mostly olivine, pyroxenes, and feldspar, but approximately a third were mixtures such as this one. Image credit: Nakamura et al. 2011

nen et al., 2004; Kohout et al., 2014; Nelson et al., 2016). In Paper III, a sample of dark volcanic sand was measured, due to its suitability as an analogue for the lunar mare regoliths. Another example is the JSC-1 lunar regolith simulant (McKay et al., 1993), which attempts to mimic the lunar mare regolith in chemical composition and grain size distribution. However, the regoliths on the lunar surface and asteroids are formed in low gravity, hard vacuum and without the presence of liquid water. Because of this, any real or analog regolith studied on the Earth is never able to exactly replicate the properties of the real surfaces.

A study by Delbo et al. (2014) suggested that rock breakup from thermal fatigue caused by an asteroid's day-night cycle can have a significant role in regolith production on asteroids. The result was based on laboratory studies of repeatedly heating and cooling meteorite fragments in a vacuum. Such a process makes the transfer of radiative energy in regolith materials a topic of even greater interest. The result has, however, also been challenged by Basilevsky et al. (2015) who argue that lunar rock samples show less thermal fatigue than the models of Delbo et al. would predict. They also question the assumptions of material loss from impacts made by Delbo et al.

1.2 Photometry of Solar System bodies

Photometry refers to the measurement of the brightness of light emitted or reflected by an object. In photometry, the light is observed over wide spectral bands, usually through standardized filters. This is in contrast to spectroscopy, where the brightness is observed as a function of wavelength at a much higher resolution. These days, photometry is almost always done with CCD cameras (Howell, 2000), but most of the data before the 1990s was acquired with photomultiplier tubes (Genet and Binzel, 1983).

There are two types of photometric observations. *Disk-resolved photometry* produces data where the observed target is practically a planar surface facet. These kinds of observations typically come from telescope images of the Moon, or *in situ* observations of Solar System objects by spacecraft cameras.

In *disk-integrated photometry* the observable is the light scattered by the entire object into the observer's direction. The light from each individual point on the object is integrated together into one value, usually because the object appears smaller than the angular resolution of the observing telescope. Ground-based asteroid photometry falls into this category.

An important quantity in light scattering in general, and Solar System photometry in particular, is the *phase angle* α, defined as the angle between the directions from the target to the light source and the observer. The term *backscattering* refers to the phase angle $\alpha = 0°$.

A Solar System object said to be in *opposition* when its geocentric longitude is 180° from the Sun. If the object is coplanar with the Earth, this corresponds to a phase angle of $\alpha = 0°$. This means that the observer sees the Sun and the object in exactly opposite directions in the sky. For example, at exactly full moon the Moon is in opposition and its phase angle is near zero. Many surfaces show an increase in brightness as they are viewed near the backscattering direction. It is also apparent in the disk-integrated photometry of small bodies near opposition. The effect is called *opposition effect* (Gehrels et al., 1964). The strength and angular width of this opposition brightening depend on the properties of the surface. It is correlated with the spectral type (Bus et al., 2002) of the asteroid, which depends on the surface mineralogy. Figure 1.7 shows a gradation of opposition effect across a range of spectral types.

There are two main causes for the opposition effect in regolith materials. The first is called the *shadowing effect* (also mutual shadowing, or the shadow-hiding opposition effect). It can be simply understood as the shadows of regolith particles obscuring other particles. When the phase angle approaches zero, the shadows are
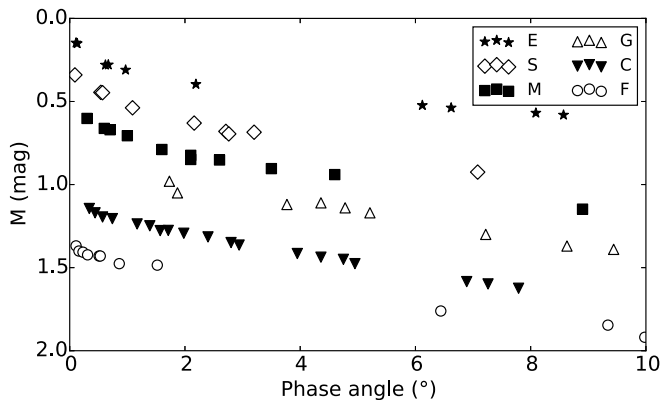
Figure 1.7: Phase curves (brightness vs. phase angle) for asteroids of six different spectral types. The asteroids in question are (64) Angelina (E-type), (20) Massalia (S-type), (55) Pandora (M-type), (1) Ceres (G-type), (24) Themis (C-type), and (419) Aurelia (F-type). The data have been shifted vertically for clarity. Data from Muinonen et al. (2015a).

hidden behind the particles and a larger proportion of lit surface can be seen.

The shadowing happens in the size regime of geometric optics. For very small particles, diffraction of the light reduces their shadows. Shepard and Campbell (1998) show that the shadowing effect is dominated by the smallest particle scale that is still large enough to effectively block light.

The other cause for opposition brightening is *coherent backscattering* (Shkuratov, 1988; Muinonen, 1989,9; Hapke et al., 1993; Hapke, 2002). It is a wave-optical effect, caused by multiple scattering in the surface. Given two scatterers A and B in the surface, the incoming light can scatter first from A to B, or vice versa. When these two beams of light combine, they interfere constructively along a cone of emergent directions, which always includes the backscattering direction. When this effect is averaged over different positions for the two scatterers, the interference is averaged out in other direction, but the constructive interference at opposition remains. The effects of shadowing and coherent backscatter combine to produce the observed opposition effect. The exact mixture of the two effects depends on the properties of the regolith.

Many Solar System bodies with an atmosphereless regolith surface have been imaged by orbiting spacecraft. Such a set of observations will consist of images taken at

various illumination geometries. A comparison of the photometric surface properties, such as albedo variations, requires that the effect of the illumination differences is reduced out of the data. This *photometric correction* requires a model that can give a reasonable value for the reflection coefficient (see Section 2.2. Also required is a way to determine the illumination geometry from the normal vector of the surface and the positions of the Sun and the camera. Domingue et al. (2016) compares the performance of different photometric models when computing the photometric corrections for spacecraft images of Mercury.

1.3 Outline of the thesis

The broad topic of this thesis are the light-scattering properties of atmosphereless bodies in the Solar System. This classification covers our Moon, most of the moons of other plants, as well as the asteroids and inactive cometary nuclei.

The thesis work specifically aimed to further develop a model for particulate surface media and apply it to questions of light scattering by various Solar System objects. This work is central to Papers I, II, and III. During the work, the author also participated in other studies relating to photometry. Results from one such line of inquiry, namely the use of ellipsoid shape models for asteroids, are presented Papers IV and V.

In Chapter 2, the most important theoretical concepts which the thesis builds on are explained. In Chapter 3, the semi-numerical Particulate Medium scattering model is described. In Chapter 4, asteroid photometry and the Lommel-Seeliger ellipsoid model are discussed. In Chapter 5, the observational data sets used in the thesis are described. Chapter 6 summarizes the papers which make up the thesis, as well as the author's contribution to them, and Chapter 7 presents concluding remarks.

2 Light scattering in the Solar System

2.1 Intensity and flux

The *intensity* of light I is defined as the amount of energy moving through a surface element dA in a time interval dt into a solid angle $d\omega$, in a direction (θ, ϕ), measured from the normal of the surface dA (Chandrasekhar, 1960; our intensity is also often called *radiance*, see Nicodemus et al., 1977).

$$dE = I(\theta, \phi) \cos\theta \, dt \, dA \, d\omega. \tag{2.1}$$

The unit of intensity is $\mathrm{Wm^{-2}sr^{-1}}$. In the present work, the surface element dA is usually a part of the surface of an asteroid or the Moon. In general the intensity is also a function of the wavelength of light; this is assumed implicitly in our notation, unless making the distinction is necessary.

The *incident flux density* πF_0 (in $\mathrm{Wm^{-2}}$) is defined as the total of power arriving to the surface element, i.e. the integral of the incident intensity over the whole in all directions,

$$\pi F_0 = \int_\Omega I(\theta, \phi) \, d\omega. \tag{2.2}$$

Illumination from a distance point source can be described as an infinitely narrow distribution of intensity,

$$I_0 = \pi F_0 \delta(\cos\theta - \cos\theta_0)\delta(\phi - \phi_0). \tag{2.3}$$

This is how the intensity of the incident radiation is defined in the present work.
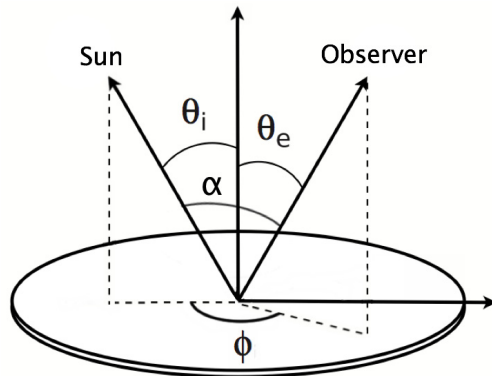
Figure 2.1: The observational geometry.

2.2 The reflection coefficient

The scattering of a surface depends on the directions of incident and emergent light. When the surface is isotropic in azimuthal angle, these directions are defined by three angles (Figure 2.1): the incidence angle θ_i, the emergence angle θ_e, and the azimuth angle ϕ. Additionally, the phase angle α is used. The phase angle can be computed from the three other angles. In many equations, the incidence and emergence angles only appear in their cosines. These cosines are denoted μ_0 and μ and are often used instead of the angles.

The intensity scattered into the direction defined by μ, μ_0 and ϕ from an incoming flux density πF_0 can be written as

$$I(\mu, \mu_0, \phi) = \mu_0 R(\mu, \mu_0, \phi) F_0, \tag{2.4}$$

where R is the *reflection coefficient*, which depends on the physical properties of the surface. Most of planetary photometry is concerned with finding the best possible approximations for R in real surfaces, and the effect of R on various observable quantities.

The reflection coefficient must obey the *reciprocity relation*, meaning that its value is the same if the incident and emergent light directions are reversed,

$$R(\mu_0, \mu, \phi) = R(\mu, \mu_0, 2\pi - \phi). \tag{2.5}$$

The simplest reflection coefficient is the Lambertian,

$$R_{\mathrm{L}} = 1. \tag{2.6}$$

Lambertian scattering describes diffuse surfaces, where the incoming flux is scattered isotropically over the entire sky hemisphere. Regolith surfaces are far from Lambertian, but it can describe, e.g., the scattering of planets with thick atmospheres. In practical measurements (Section 5.2), the reflection coefficient of a surface cannot be measured directly. Instead, the ratio of intensities between the surface and a standard material approximating Lambertian scattering is measured.

Another important case are semi-infinite homogeneous media, where a light beam is exponentially attenuated and scatters once with a single-scattering phase function $P(\alpha)$ and single-scattering albedo $\tilde{\omega}$. If the single-scattering albedo is low, higher orders of scattering can be neglected. For this case, radiative transfer theory leads to the Lommel-Seeliger reflection coefficient (Fairbairn, 2005),

$$R_{\mathrm{LS}} = \frac{1}{4}\tilde{\omega}P(\alpha)\frac{1}{\mu + \mu_0}. \tag{2.7}$$

Lommel-Seeliger scattering has long been used for the photometry of dark surfaces, e.g. the brightness distribution over the Lunar disk and asteroids.

2.3 Disk-integrated brightness

There are hundreds of thousands of small bodies (asteroids and comets) which have been observed by observatories on the Earth. All but a few of these objects are too small to resolve by even the most powerful telescopes. Therefore the vast majority of data on Solar System objects in the visual wavelengths are in the form of *disk-integrated brightness*.

The disk-integrated brightness L is defined as the integral of the intensity over the lit and visible parts of the surface,

$$L = \int \mu\mu_0 R(\mu, \mu_0, \alpha)F_0 \, \mathrm{d}A. \tag{2.8}$$

The unit of disk-integrated brightness is therefore W/sr. For a convex body, the lit and visible surface consists of the points for which $\mu > 0$ and $\mu_0 > 0$. For non-convex bodies, the situation is more complex since parts of the surface can obstruct other

parts. In general, the disk-integrated brightness of a non-convex body cannot be computed analytically, and methods such as ray tracing are needed.

A flat disk with Lambertian scattering is used as a comparison in many situations, such as the definition of the geometric albedo (below). The disk-integrated brightness of a Lambertian disk with diameter D is

$$L_{\mathrm{Ld}}(\alpha) = \frac{\pi}{4} D^2 F_0 \cos \alpha \qquad (2.9)$$

The simplest three-dimensional body is the sphere. The disk-integrated brightness for a Lommel-Seeliger scattering sphere with diameter D is

$$L_{\mathrm{LS}}(\alpha) = \frac{1}{32} \pi F_0 D^2 \tilde{\omega} P(\alpha) \left(1 - \sin \frac{\alpha}{2} \tan \frac{\alpha}{2} \log \left(\cot \frac{\alpha}{4} \right) \right). \qquad (2.10)$$

An analytical solution has also been recently demonstrated for a Lommel-Seeliger scattering triaxial ellipsoid (Muinonen and Lumme, 2015). It is used in Papers IV and V. However, its mathematical form is lengthy and therefore not repeated here.

2.4 Nomenclature of phase functions

There are three different kinds of functions of the phase angle which are relevant to the present work. Their differences can lead to some confusion, so they are explicitly defined here.

First, the disk-integrated brightness function $L(\alpha)$, defined above, is an absolute measure of the energy scattered by the whole object into the observer's direction.

Second, phase functions denoted with a capital P, such as a single-scattering phase function $P(\alpha)$ are understood to be unitless and normalized over the full sphere of scattering,

$$\int_\Omega \frac{P(\alpha)}{4\pi} \, \mathrm{d}\Omega = \int_0^{2\pi} \int_0^\pi \frac{(\alpha)}{4\pi} \sin \alpha \, \mathrm{d}\alpha \, \mathrm{d}\phi = 1. \qquad (2.11)$$

Third, phase functions denoted $\Phi(\alpha)$ are also unitless, but normalized to unity at $\alpha = 0°$,

$$\Phi(\alpha) = \frac{f(\alpha)}{f(0°)}, \qquad (2.12)$$

where f is some function of the phase angle.

2.5   Geometric, planar, and spherical albedo

The geometric albedo p is defined as the ratio between the integrated brightness of the body at zero phase angle and the integrated brightness of a Lambertian disk with the same equivalent diameter D.

$$p = \frac{L(0°)}{L_{\mathrm{Ld}}(0°)} = 4\frac{L(0°)}{\pi D^2 F_0}. \tag{2.13}$$

For Lommel-Seeliger scattering, any curved surface appears identical to its planar projection at zero phase angle. Therefore, the geometric albedo p is a constant depending only on the phase function and single-scattering albedo, i.e. the properties of the surface material. The scattering of real regoliths on the Moon, as well as our semi-numerical scattering model (Chapter 3) also exhibit this property.

The planar albedo A_p is the fraction of incident flux scattered into all directions in the sky hemisphere by a planar surface element dA, as a function of the incident direction μ_0,

$$A_p(\mu_0) = \int_0^1 \int_0^{2\pi} \mu\mu_0 R(\mu, \mu_0, \phi)\, \mathrm{d}\phi\, \mathrm{d}\mu. \tag{2.14}$$

The spherical albedo A_s is the fraction of the incident flux scattered into all directions by the whole surface,

$$A_s = \frac{\int \mu\mu_0 F_0 R(\mu, \mu_0, \phi)\, \mathrm{d}A}{\int \mu_0 F_0\, \mathrm{d}A} \tag{2.15}$$

where the integration over is done over the lit part of the surface. Like the integrated brightness, this integral is generally difficult to compute for non-convex bodies.

A Lommel-Seeliger sphere has a geometric albedo of $p_{LS} = \frac{\omega}{8}$, and a spherical albedo of $A_{LS} = \frac{2}{3}(1 - \log 2)$.

2.6   Scattering models for planetary regoliths

Various models for the reflection properties of planetary regoliths have been developed during the last century. A review of current models is found in Li et al. (2015). The Lommel-Seeliger model (Equation 2.7) is one of the oldest, having been used in

Solar System photometry since the late 19th century. With a suitable phase function, it provides a reasonable fit to the photometry of most dark regolith surfaces.

The Hapke model (e.g., Hapke, 1981, 2002) is perhaps the most widely used reflectance model. It was introduced in the 1980s and has had many modifications and additions since then to better account for phenomena such as shadowing and coherent backscatter. The model is capable of describing the reflectance of many different kinds of surfaces. It has, however, also been criticized for having a large number of free parameters, especially in its most developed forms, and for providing best-fit parameters for observed surfaces which are not always physically credible. Shepard and Helfenstein (2007) tested the Hapke model with laboratory samples and found little evidence that the model parameters correspond to real parameters of the sample. Later Helfenstein and Shepard (2011) tested a newer version of the Hapke model and found that the estimation of porosity in dark samples was improved, though they made no strong conclusions due to their small number of test cases.

Other scattering models for planetary surfaces include, e.g., those by Minnaert (1941), Lumme and Bowell (1981), and Shkuratov (1999). They lack the status of wide use which the Hapke model has gained in the remote sensing community, but are still valid models with potential applications. For example Domingue et al. (2016) find that the Shkuratov model performs better than the Hapke model in the photometric correction of orbital images of the surface of Mercury.

3 The Particulate Medium scattering model

We implement a semi-numerical scattering model for particulate surfaces, (Paper II). We call it the Particulate Medium (or PM) scattering model. The reflection coefficient for the PM model is

$$R_{\mathrm{PM}} = \frac{1}{4}\omega_V P_V(\alpha) S(\mu, \mu_0, \phi)\frac{1}{\mu + \mu_0}.$$ (3.1)

This resembles the Lommel-Seeliger model, with the addition of a new term S, which we call the *shadowing correction*, and the replacement of the single-scattering albedo $\tilde{\omega}$ with the *volume-element albedo* ω_V and the single-scattering phase function with the *volume-element phase function*. These quantities are abstractions of more complicated scattering phenomena inside a small volume element of the surface, which is still large compared to the wavelength of the scattered light. The volume element is taken to describe the scattering of a single regolith grain and its immediate surroundings, while the S term describes the mutual shadowing effects between volume elements. The shadowing correction S has a maximum value of 2 at opposition.

3.1   Computing the shadowing correction

The shadowing correction S in Equation 3.1 can be derived numerically through a ray-tracing simulation. This approach requires significant computational resources with the current software, but can be pre-computed over a grid of illumination geometries and re-used later. This pre-computation of reflection coefficient values is presented in Paper II. Here we only give a brief overview of the method and refer to that paper for a more detailed description of the model.

The simulated medium consists of a large number of spheres with an arbitrary size distribution. The current set of pre-computed values uses a uniform distribution
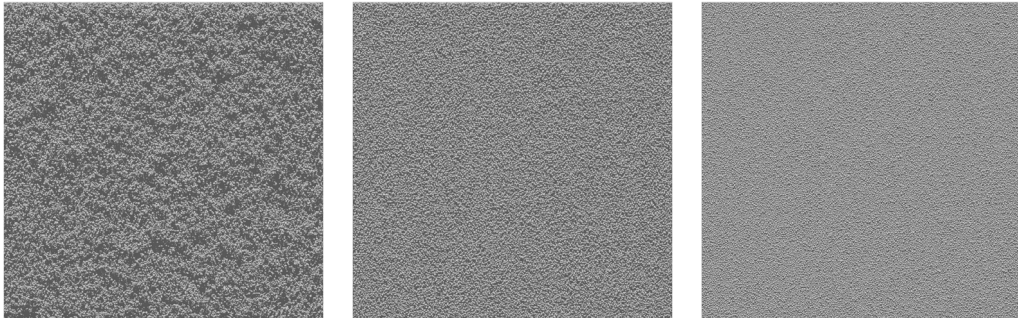
17

Figure 3.1: A visualization of a simulated slab of spheres with packing density $\nu = 0.15$, 0.30 and 0.55. The viewing is straight from the zenith and the illumination is from a $45°$ angle.

in particle diameter, but a monodisperse (all spheres are the same size) and log-normal distribution are also possible. The medium is created with a sphere-dropping algorithm, in which spheres are added into the simulation box from above, one by one and each drop is either accepted or repeated. By changing the acceptance criterion of the sphere drops, the packing density of the medium can be chosen. The media are created thick enough that no rays in the simulation can penetrate through the entire volume.

Macro-scale (i.e. larger than the single-particle scale) surface roughness is also added before the ray-tracing. The macro-scale roughness takes the form of a random surface with *fractional Brownian motion* (fBm) statistics, which intersects the simulation box. This surface is created by first generating its two-dimensional power spectrum, with desired statistics, and then inverting that into a height map with the inverse Fourier transform. Spheres above the surface are removed from the simulation, producing a rough top surface.

A ray-tracing simulation is used to produce an approximation of Equation 3.1 in a standard situation: The spheres in the simulation medium are given a Lommel-Seeliger scattering surface in the simulation. The whole simulation is then treated as a PM scattering model, based on individual scatterers with the phase function of a Lommel-Seeliger sphere. The Lommel-Seeliger phase function can be divided out of the result, and the shadowing correction S separated. Discrete values of the S functions can then be precomputed into tables loaded into software. In practice, it is easier to tabulate the whole R_{PM} with an isotropic phase function. To get the final

value in a given illumination geometry, it is then enough to look up the precomputed value and multiply it with the value of the desired phase functions.

The shadowing correction is computed as a function of three parameters. The most significant one is the packing density ν, which is defined as the ratio between the volume occupied by particles to the bulk volume. The range of packing densities used in the computations is 0.15 to 0.55, at intervals of 0.05.

The macro-scale roughness added to the surface has two parameters. The Hurst exponent $\mathcal{H}$ determines fractal statistics of the surface. It is analogous to the correlation distance for a Gaussian random surface in determining the horizontal scale of variations in the roughness. A low $\mathcal{H}$ means a short correlation and a "spiky" surface, while a high $\mathcal{H}$ produces wide and smooth undulations. We vary $\mathcal{H}$ from 0.2 to 0.8. The roughness amplitude σ is the maximum amplitude of the random field, in simulation units. The amplitude in our study varies from zero to 0.10.

3.2 Photometric properties of the PM model

The PM model resembles the Lommel-Seeliger model in form, but the shadowing correction changes the resulting reflection coefficient significantly. The effects of the shadowing correction are largely a function of phase angle, but there are significant azimuthal effects as well. A purely phase-angle-dependent term is unable to describe these well. Figure 3.2 shows an example of the reflection coefficient values of the PM model for three different values of the packing density ν as the surface roughness is varied. It is clear that for the very loosely packed medium, the addition of surface roughness does not change the shadowing correction significantly, while for the densest-packed medium the differences due to roughness can be dramatic.

Due to the Monte Carlo computation of the shadowing correction, there is some amount of noise in the final values of the scattering model. In theory this noise can be made arbitrarily low by increasing the computational effort spent on the shadowing correction. In practice, the effort needed becomes unfeasible with the current version of the ray-tracing software used. In situations with real observed or measured data, the noise level of the current set of pre-calculated shadowing corrections is usually lower than the noise in the observed data.

A sphere with the PM scattering model has a geometric albedo of $p_{PM} = \frac{1}{4}\omega_V P_V(0°)$. The integrated brightness and the spherical albedo depend on the model parameters and must be computed numerically. A software package has been developed to compute the photometric properties of spheres and arbitrary triangulated shapes with a given PM scattering model.

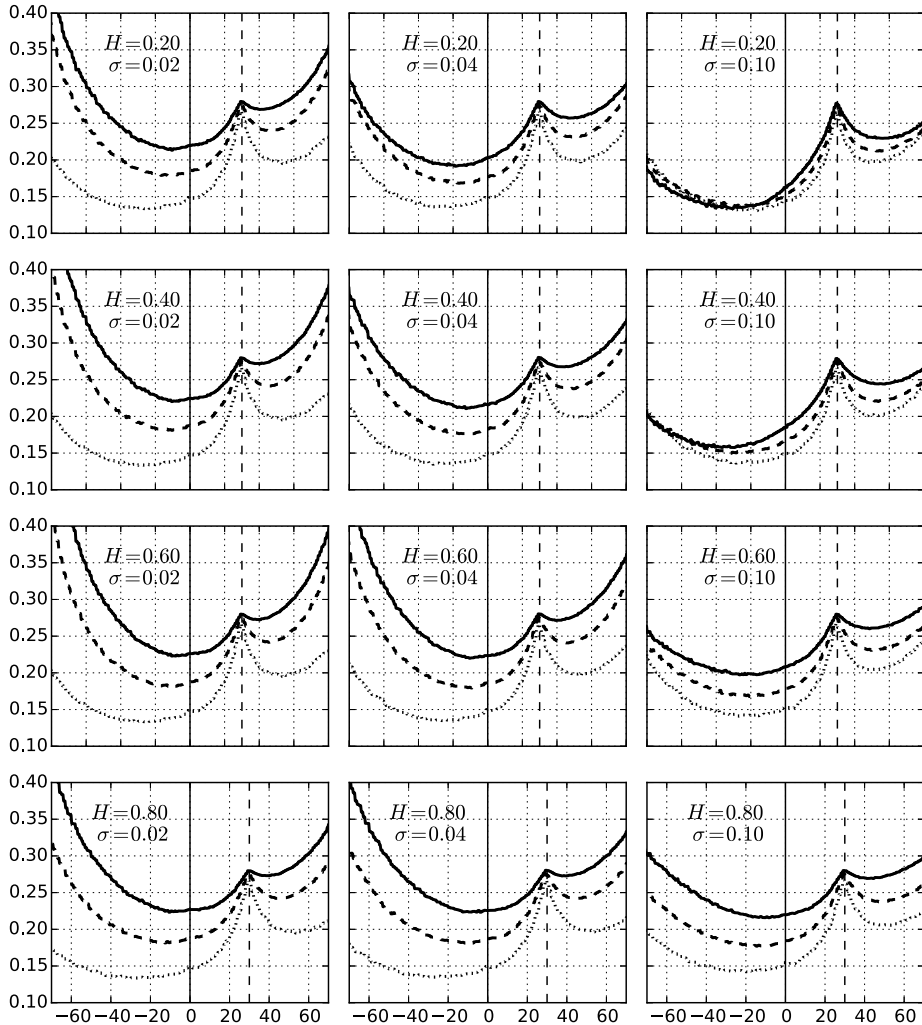Figure 3.2: The value of the PM scattering model as a function of the emergence angle at $\phi = 0°$ and $30°$ incidence, with an isotropic phase function, $P_V(\alpha) = 1$. The values for three different packing densities are shown: $\nu = 0.55$ (solid line), $\nu = 0.30$ (dashed line), and $\nu = 0.15$ (dotted line). The surface roughness parameters H and σ are indicated on the panels.

4 Asteroid photometry

4.1   Lightcurve observations

A *lightcurve* is a series of photometric observations as a function of time. Each observation is the integrated brightness of the asteroid (Equation 2.8). Usually the observational geometry is also given by the position vectors of the asteroid and the Earth in a heliocentric system, or equivalent.

Broadly speaking, a *dense lightcurve* is one where the interval between observations is small compared to the rotation period of the asteroid. Practically this means that observations are taken during a single night, with the intervals measured in minutes. Dense lightcurves require dedicated campaigns designed to observe the same object repeatedly.

The opposite is a *sparse lightcurve*, where the observations are scattered across wide intervals, with often days or months between observations. These kinds of observations are typically byproducts of surveys, such as the primarily astrometric ESA Gaia mission (Mignard et al., 2008), which observe the sky in a systematic way, but only detect any individual object by chance. The interpretation of sparse data is generally more difficult and require specialized methods.

4.2   Lightcurve inversion

A lightcurve depends on the rotational state, shape, and albedo variations of the asteroid. This means that, in theory, it is possible to get information on these properties by studying the lightcurves. In recent decades, through advances in the studies of inverse problems and the improvements in computer resources and algorithms, this theoretical possibility has become a practical reality. The shape and rotational state are important constraints on the physical properties of the asteroid as a whole. Being able to estimate these well from ground-based photometry, our most abundant data source for asteroids, brings large gains for our knowledge of the asteroid population.

The determination of the shape of an asteroid from its lightcurve was deemed

impossible by Russell (1906), who limited his approach only to the opposition geometry. This overly pessimistic view persisted for almost a century and was repeated by, e.g., Groeneveld and Kuiper (1954). The lack of good data was another discouraging factor. During the 20th century, shape modelling was mostly done with simple shape models, such as ellipsoids (Magnusson et al., 1989).

The theoretical basis for more refined shape inversion from lightcurve data was introduced by Kaasalainen et al. (1992). A rigorous mathematical approach by Kaasalainen and Lamberg (2006) proved a number of theorems about the requirements and limits of observational data in a generalized form of the problem. In short, having a wide selection of lightcurves in different observational geometries, especially at larger phase angles, allows the construction of shape models.

The practical methods for lightcurve inversion were developed by Kaasalainen and Torppa (2001) and Kaasalainen et al. (2001). Convex shape inversion was found to be relatively easy, given good enough data. In their simulations, convex shape models from lightcurve data resemble the convex hulls of the real asteroid shape.

As the amount of observational data has grown at an increasing rate, convex shape determinations are now routinely done for many asteroids. Non-convex shape models, which require significantly better data, still remain rare. For a review on photometric methods in asteroid shape and rotation modelling, see Kaasalainen et al. (2002). For a more recent review focusing on other data sources to supplement the photometry, see Durech et al. (2015).

4.3 Lommel-Seeliger ellipsoids

Muinonen and Lumme (2015) presented an analytical solution to the disk-integrated brightness of a triaxial ellipsoid with the Lommel-Seeliger scattering model. This enables much faster computation of lightcurves for an elliptical object. The triaxial ellipsoid model is a useful first step in shape model development, since it provides a rough estimate for the overall shape, and only has two free parameters, the axis ratios b/a and c/a.

Cellino et al. (2015) and Muinonen et al. (2015b, Paper IV) have applied the analytical solution to solve for ellipsoid shape models of asteroids with very sparse observational data, such as will be provided by the ESA Gaia astrometric space telescope. The data used in the studies were artificial observations simulating Gaia data, as well as sparse ground-based photometry. The Lommel-Seeliger ellipsoids are found to provide good first approximations for the true axial ratios of the asteroids in most of the test cases.

Figure 4.1: The three shape models used to study the effect of the PM model on disk-integrated photometry. From left: (951) Gaspra, (433) Eros and (216) Kleopatra. Their relative sizes are not to scale.

In Paper V (Muinonen and Wilkman, 2016), the ellipsoid shape model is used to compute the Bond albedos (Equation 2.15) for ellipsoidal asteroids. It is found that the Bond albedo depends on the orientation of the asteroid towards the light source. The albedo of an ellipsoid is both lower and higher than that of a sphere, depending on the orientation. The variation of the albedo depends on the axial ratios of the ellipsoid and can be on the order of 10%.

4.4   Applying the PM model to asteroid photometry

We have also applied the PM model in asteroid photometry. The aim was to study the effects of a non-convex shape and the choice of scattering model on asteroid photometric properties and lightcurves. The results presented in this section are as yet unpublished.

Lightcurves were computed for three accurate non-convex asteroid shape models (Figure 4.1) representing (951) Gaspra, (433) Eros and (216) Kleopatra. The shapes of these asteroids are known from *in situ* observations from the Galileo and NEAR-Shoemaker missions in the case of Gaspra and Eros (Stooke, 1997; Thomas et al., 2002), and from radar observations at Arecibo in the case of Kleopatra (Ostro, 2000).

The three shape models span a range of non-convexity: Gaspra is relatively convex, with some craters and depressions around its middle. Eros is a banana-like curved shape, and has a large crater on one side. Kleopatra is a dog-bone shape, with two bulges connected by a narrower neck.
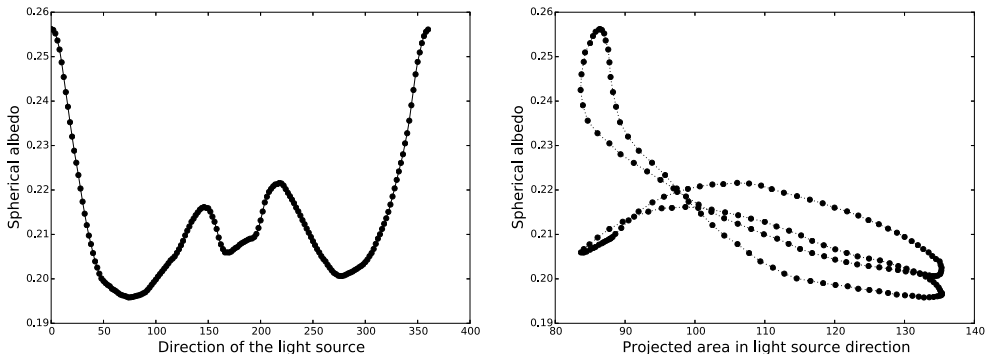
Figure 4.2: Left: The spherical albedo of the Gaspra shape model with a PM scattering model with low packing density and no surface roughness, as a function of the light source direction around the asteroid's equator. Right: the spherical albedo plotted against the cross section area in the direction of the light source.

The simulated lightcurves were computed in idealized observation geometries: the distance from the asteroid to both the Sun and the Earth was set to 1 AU, and the phase angle was changed by rotating the solar direction. Seven different spin axis directions were used.

It is generally thought that the exact choice of scattering model does not affect asteroid lightcurves or shape determination significantly (e.g Kaasalainen et al., 2001; Kaasalainen and Lamberg, 2006), as long as it is "realistic enough". Our results with the Particulate Medium model agree with this. When the same phase function and geometric albedo are used, in most cases the differences in computed brightness between the PM model and Lommel-Seeliger was small.

The most interesting features are found in the dependence of the spherical albedo on the shape of the body and the direction of illumination. Figure 4.2 shows how the spherical albedo of the Gaspra shape model changes as a function of the illumination direction. The relationship between the spherical albedo and the projected cross-section in the light source direction is also complicated. For an ellipsoid body, this curve is a straight line, with high albedo corresponding to small cross-section. This is due to the higher angles of incidence presented by the narrow end of the ellipsoid. For the complicated non-convex shape models, the shape of the curve spreads out and can vary wildly. It also depends on the scattering model parameters to some extent, but the effect of the shape is greater.

5 The PM model and disk-resolved photometry

5.1   Lunar photometry from SMART-1/AMIE

In Paper I (Wilkman et al., 2014), the PM scattering model is applied to disk-resolved photometry of the lunar surface, obtained from images taken by the SMART-1 spacecraft.

The European Space Agency's *Small Missions for Advanced Research in Technology-1* (SMART-1) was the first European spacecraft to orbit the Moon. It was launched in 2003 and orbited the Moon in 2004–2006. It featured many advanced and experimental technologies, such as ion propulsion and a slow but fuel-efficient transfer orbit from the Earth to the Moon (Racca et al., 2002). Most of the scientific instruments of the mission were novel designs, some of which have been the basis of later instruments on other missions.

SMART-1 studied the lunar surface from an elliptical orbit with the periapsis 500 km above the south pole and apoapsis 3000 km above the north pole. The optical camera on board was called AMIE (Advanced Moon micro-Imager Experiment). It was a 1024×1024 pixel CCD camera with various colour filters permanently installed on the detector. The typical pixel resolution of the surface photographs was 50–200 metres/pixel (Grieger et al., 2008).

The disk-resolved photometry of the darker lunar mare regions was acquired from the AMIE data archives. The images were chosen to represent smooth areas of various lunar maria, avoiding large craters and other large topographic features. Only images with the "clear" filter were used.

Several 10×10 pixel samples were chosen by hand from each AMIE image. The samples were again chosen to avoid topographic features visible at the scale of the images. Using a model of the spacecraft location and orientation at the time of each image, and assuming an elliptical surface for the Moon, the illumination geometry for each sample was estimated. The pixel values in each sample were averaged to
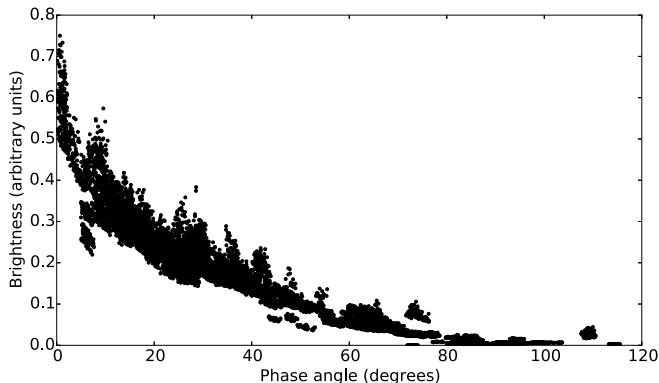
Figure 5.1: The photometry data extracted from the AMIE images as a function of phase angle.

get the intensity value for that sample. The AMIE dataset does not have absolute calibration, but the values between different images should be comparable.

In total the data set has 16 776 data points, mostly at moderate solar phase angles (10–30°), but ranging from almost zero phase angle to 110°. The quality of the data is rather poor, however, with large uncertainties and clear outliers (probably due to albedo variations).

5.2   Laboratory measurements with FIGIFIGO

The Finnish Geodetic Institute Field Goniometer (Suomalainen et al., 2009; Peltoniemi et al., 2014) is a portable spectro-goniometer. It can measure the reflection coefficient of a surface under different illumination geometries, as a function of wavelength from visible to near-infrared (NIR). It is owned by the Finnish Geospatial Research Institute (FGI; formerly the Finnish Geodetic Institute).

The device consists of a spectrometer connected by optical fibre to focusing optics at the end of a long arm. The arm can be turned around two axes to change the emergence angle and the azimuth angle. The incidence angle can be chosen by adjusting an artificial light source in the laboratory, or by waiting for the solar zenith angle to change when measuring outdoors. The reflection coefficient is obtained by first measuring the brightness of the target surface. This is then divided by the brightness of a reference material which approximates Lambertian scattering.

For Paper III, measurements of dark volcanic sand (Figure 5.2, left) were performed in the laboratory at the FGI. These measurements were used to test the PM model's ability to fit accurate laboratory measurements of the reflection coefficient of a dark regolith-like material.

The measured sample was treated in different ways to produce qualitatively different surface roughness. Two wide spectral bands at 500–600 nm and 800-900 nm were used for the analysis. The volume-element albedo and phase function of the PM model were assumed to depend only on the spectral band and not on the sample treatment. Conversely, the shadowing correction was assumed to depend only on the sample treatment but be same for all spectral bands. There were a total of four sample treatments, therefore the eight combinations of two phase functions and four spectral bands were fit.

The fit results were promising (Figure 5.2, right). The PM model provided a close fit to reflection features at all azimuthal angles, across the eight different fits. The interpretation of the PM model parameters in terms of the real properties of the sample remains vague, however, since the characterization of the samples was only qualitative.

The same analysis was also performed with the Lommel-Seeliger scattering model, which failed to perform equally well, as was expected. The real data contain azimuthal effects arising from the particulate nature of the material, which the L-S model does not take into account. The largest discrepancies of the L-S model were found at high azimuthal angles and the least compacted samples, where the shadowing effects would be strongest.
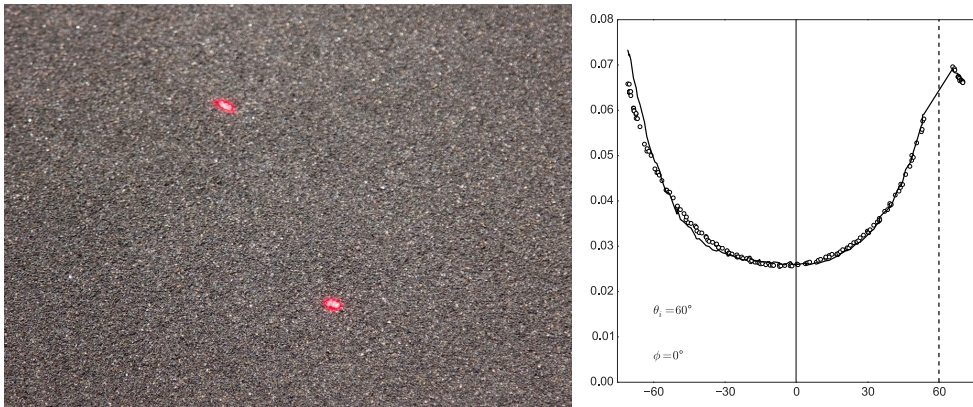
Figure 5.2: A photograph of the volcanic sand sample measured with FIGIFIGO, and a plot of its reflection coefficient in the principal plane (white dots), together with the PM model fit curve. On the sample, the two laser dots are approximately 10 centimetres apart. The dashed vertical line indicates the light source direction.

6 Summary of the publications

The thesis consists of the following publications:

- **Paper I**: **Wilkman, O.**, Muinonen, K., Videen, G., Josset, J.-L., & Souchon, A. (2014). Lunar photometric modelling with SMART-1/AMIE imaging data. Journal of Quantitative Spectroscopy and Radiative Transfer, 146, 529–539. doi:10.1016/j.jqsrt.2014.01.015T

- **Paper II**: **Wilkman, O.**, Muinonen, K. & Peltoniemi, J. (2015). Photometry of dark atmosphereless planetary bodies: an efficient numerical model. Planetary and Space Science. doi:10.1016/j.pss.2015.06.004

- **Paper III: Wilkman, O.**, Gritsevits, M., Zubko, N., Peltoniemi, J. & Muinonen, K. (2016). Photometric modelling for laboratory measurements of dark volcanic ash. Journal of Quantitative Spectroscopy and Radiative Transfer (submitted)

- **Paper IV**: Muinonen, K. O., **Wilkman, O. V.**, Cellino, A., Wang, X. & Wang, Y. (2015). Asteroid lightcurve inversion with Lommel–Seeliger ellipsoids. Planetary and Space Science 118, pp. 227–214

- **Paper V**: Muinonen, K. O. & **Wilkman, O. V.** (2016). Spherical albedo of a Lommel-Seeliger scattering ellipsoidal asteroid, Proceedings of the International Astronomical Union, Symposium S318, Asteroids: New Observations, New Models. Chesley, S., Morbidelli, A. & Jedicke, R. (ed.). Cambridge University Press

The papers are summarised below. The author's contribution to the papers is described in Section 6.6.

6.1 Paper I

In Paper I, we extracted disk-resolved photometric data from CCD images of the lunar surface taken by the SMART-1 spacecraft. The data represented the lunar mare regions, which are flat in topography and have a low albedo. The illumination geometry of each photometric data point was estimated using the known spacecraft position and assuming the surface to be flat.

We used the particulate medium scattering model to fit these data. The results show that the PM model can provide good fits to photometric data of a dark regolith-covered Solar System body. However, the work was limited to broad conclusions. Better fits were acquired with lower packing densities in the model. Even the lowest packing density was unable to produce a strong enough opposition effect by itself, so a volume-element phase function with a significant opposition spike was needed. This is more evidence for the already well-established hypothesis that the lunar opposition effect is not caused by just shadowing effects.

6.2 Paper II

In Paper II, we present the particulate medium scattering model in detail. It consists mostly of a description of the PM model similar to the one in Chapter 3. The numerically computed data for the PM model are made publicly available and an example of its usage for asteroid photometry is given.

6.3 Paper III

In Paper III, we applied the PM scattering model to laboratory measurements of a dark volcanic basalt sand. The material is an analogue to the dark basaltic regolith of the lunar mare regions, and a possible analogue to the regoliths of dark asteroids. The measurements were performed with the FIGIFIGO spectro-goniometer at the FGI laboratory in Masala, Finland. The same sample of volcanic sand was measured three times with a different treatment of the sample each time, in an attempt to alter the surface roughness and packing properties of the material.

The PM model proved able to fit the observed data very well, though the interpretation of the model parameters is still somewhat uncertain. By varying the volume-element phase function in different spectral bands, spectral differences could be accounted for, and the material was shown to be more backward scattering in the

NIR band (around 850 nm) and forward scattering at shorter wavelengths (around 550 nm).

6.4 Paper IV

In Paper IV, we use the analytical solution for the disk-integrated brightness of a Lommel-Seeliger ellipsoid (Section 4.3) to produce spin and shape models from asteroid lightcurves. The approached used in the study consisted of multiple stages: first a preliminary spin period was obtained with a rough initial shape and spin axis distribution. Secondly, the spin axis direction was then estimated with higher resolution, after which a non-linear least-squares solution to the full spin and shape model was determined. Finally a Markov chain Monte Carlo approach was used to obtain a posterior distribution for the parameter values, which describes the uncertainty of the estimates.

Two kinds of lightcurve data were studied: simulated sparse lightcurves, made to resemble the kind of asteroid photometry obtained by the ESA Gaia mission, as well as dense ground-based lightcurves of real asteroids. The photometry for the simulated Gaia data was generated using the PM scattering model introduced in Paper II.

6.5 Paper V

In Paper V, we studied the spherical and geometric albedos of ellipsoid shape models with the Lommel-Seeliger scattering model. The analytical solution for the integrated brightness of a Lommel-Seeliger ellipsoid by Muinonen and Lumme (2015) was used, along with a realistic asteroid phase function. We showed that the shape and rotational state of the asteroid can affect the spherical albedo by almost 10%.

6.6 Author's contribution to the papers

In Paper I, the author performed the extraction of the photometric data from the photographs, computed the ray-traced values for the PM scattering model, using a modification of the software by Parviainen and Muinonen (2009), wrote the software to fit the model in the data, wrote most of the text, and made all the figures and in the paper, except Figure 1, which is from Parviainen et al.

In Paper II, the author developed further the ray-tracing software for the PM model, pre-computed the scattering model values, made most of the figures and wrote

most of the text.

In Paper III, the author participated in the laboratory measurements, performed the model fitting and comparisons, made all the figures, and wrote most of the text.

In Paper IV, the author performed part of the shape model computations, created most of the figures and wrote parts of the Results section. The author also prepared the PM model which was used to generate the simulated Gaia photometry.

In Paper V, the author aggregated the computed albedo values in order to derive the conclusions of the paper, created most of the figures and wrote most of the Results and Discussion section.

6.7 Publications not included in the thesis

In addition the the five papers included in the thesis, the author has also contributed to the following two papers:

- **Wilkman, O.**, & Muinonen, K. (2014). Asteroid lightcurve phase shift from rough-surface shadowing. Meteoritics & Planetary Science, 49(1), 1–7.

- Penttilä, A., Schevchenko, V. G., **Wilkman, O.** & Muinonen, K. (2015). H, G_1, G_2 photometric phase function extended to low-accuracy data. Planetary and Space Science, in press, doi:10.1016/j.pss.2015.08.010

The main results of the first paper were found to be erroneous due to a programming error, and a corrigendum has been issued in MAPS redacting the results.

The second paper presents improvements to the H, G_1, G_2 magnitude system which is used to describe asteroid phase curves. The author wrote a software package in Python for the fitting of the H, G_1, G_2 model to observational data, but did not contribute to the main results or the text of the paper.

7 Concluding remarks

The core of the thesis work was the PM scattering model, and its application to planetary photometry. Papers I and III show that the model can describe disk-resolved photometry of regolith surfaces well. The model is able to reproduce azimuthal features in the observed data, which the Lommel-Seeliger model is incapable of. This shows that the shadowing effects in a particulate surface cannot be fully described with terms that depend only on the incidence and emergence angles and the phase angle, without considering the azimuth angle explicitly.

The results described in Section 4.4 indicate that in disk-integrated photometry the significance is much smaller. However, the PM model can also be useful in making simulated lightcurves for testing other models, such as the Lommel-Seeliger ellipsoids. This way, the data is generated by an independent model and the so called "inverse crime" is avoided. The PM model continues to be used for this purpose.

The PM model could be used to derive photometric corrections for orbital images of planetary surfaces, though such work has not yet been attempted. This requires making some assumptions as to the PM model parameters describing the surface. These could possibly be derived in an average sense from the images themselves.

Surfaces can be characterized in terms of their PM model parameters, though the connection between the parameters of the PM model, and the parameters of a real regolith material remain vague. In particular, the effect of the size distribution in the simulation is not well studied. More comparison work with laboratory measurements would be necessary, with more carefully controlled samples. Samples sieved to narrower and better controlled size distributions would be especially useful. The packing density and surface roughness of a laboratory sample are also very difficult to characterize quantitatively. These kinds of problems are common to all scattering models.

All of the work with the PM model is complicated by the need for heavy precomputation. This need also limits the accuracy and angular resolution of the model. The most significant developments of the model to increase its usefulness would be in accelerating the process. Modern real-time computer graphics, accelerated by

external graphics processing units (GPU), the ray-tracing process used to derive the PM model could be made considerably faster.

Possible steps towards a faster computation, in order of growing effort, include: first reducing the number of particles used in the simulation, looking for a compromise between a large enough simulation volume and low enough memory usage and intersection-finding time of the ray-tracing code. Second, rewrite the whole intersection-finding code with a more effective algorithm. This is likely to require also changes in the way that the simulation medium is represented in memory. Third, implement this algorithm with GPU acceleration, as such computation is exactly what GPUs are made for. Another route would be to parallelize the code more effectively. Such a Monte Carlo ray-tracing problem is technically called "embarrassingly parallel", i.e. individual repetitions are totally independent. However, the memory usage and shared data structures complicate the large-scale parallelization of the code in its current form. Steps in this direction have been taken.

The analytical integrated brightness solution for Lommel-Seeliger ellipsoids, used in Papers IV and V, is a promising tool for coarse asteroid shape modelling. Faster algorithms for rough shape and spin estimation from lower-quality data are important, as surveys produce sparse lightcurves of asteroids that happen to be in their fields.

References

Basilevsky, A. T., Head, J. W., Horz, F., and Ramsley, K. Survival times of meter-sized rock boulders on the surface of airless bodies. *Planetary and Space Science*, 117:312–328, 2015. 10.1016/j.pss.2015.07.003.

Burbine, T. H., McCoy, T. J., Meibom, A., Gladman, B., and Keil, K. Meteoritic Parent Bodies: Their Number and Identification. In Bottke, W. F. J., Cellino, A., Paolicchi, P., and Binzel, R., editors, *Asteroids III*. University of Arizona Press, Tucson, AZ, 2002.

Bus, S. J., Vilas, F., and Barucci, M. A. Visible-Wavelength Spectroscopy of Asteroids. *Asteroids III*, 2002.

Cellino, A., Muinonen, K., Hestroffer, D., and Carbognani, A. Inversion of sparse photometric data of asteroids using triaxial ellipsoid shape models and a Lommel-Seeliger scattering law. *Planetary and Space Science*, submitted, 2015.

Chandrasekhar, S. *Radiative Transfer*. Dover Publications, Inc., New York, 1960.

Clark, B. E. Asteroid Space Weathering and Regolith Evolution. In Bottke, W. F. J., Cellino, A., Paolicchi, P., and Binzel, R., editors, *Asteroids III*, pages 585–599. University of Arizona Press, Tucson, AZ, 2002. 10.1016/0273-1177(91)90551-T.

Delbo, M., Libourel, G., Wilkerson, J., Murdoch, N., Michel, P., Ramesh, K. T., Ganino, C., Verati, C., and Marchi, S. Thermal fatigue as the origin of regolith on small asteroids. *Nature*, 508(7495):233–6, 2014. 10.1038/nature13153.

Domingue, D. L., Denevi, B. W., Murchie, S. L., and Hash, C. D. Application of multiple photometric models to disk-resolved measurements of Mercury's surface: Insights into Mercury's regolith characteristics. *Icarus*, 268:172–203, 2016. 10.1016/j.icarus.2015.11.040.

REFERENCES

Durech, J., Carry, B., Delbo, M., Kaasalainen, M., and Viikinkoski, M. Asteroid Models from Multiple Data Sources. In Michel, P., DeMeo, F., and Bottke, W. F., editors, *Asteroids IV*. University of Arizona Press, 2015.

Fairbairn, M. P. Planetary Photometry: the Lommel-Seeliger law. *Journal of the Royal Astronomical Society of Canada*, 99, 2005.

Gaffey, M. J. Space weathering and the interpretation of asteroid reflectance spectra. *Icarus*, 209(2):564–574, 2010. 10.1016/j.icarus.2010.05.006.

Gehrels, T., Coffeen, T., and Owings, D. Wavelength dependence of polarization. III. The lunar surface. *The Astronomical Journal*, 69:826, 1964. 10.1086/109359.

Genet, R. and Binzel, R. P. *Solar system photometry handbook*. Richmond, 1983.

Grieger, B., Foing, B. H., Koschny, D., Beauvivre, S., Pinet, P., Cerroni, P., Sanctis, M. C. D., Barucci, M. A., et al. Coverage and pointing accuracy of SMART-1/AMIE images. In *Lunar and Planetary Science XXXIX*. 2008.

Groeneveld, I. and Kuiper, G. P. Photometric Studies of Asteroids. I. *The Astrophysical Journal*, 120:200, 1954. 10.1086/145904.

Hapke, B. Bidirectional reflectance spectroscopy: 1. Theory. *Journal of Geophysical Research: Solid Earth*, 86(B4):3039–3054, 1981. 10.1029/JB086iB04p03039.

Hapke, B. Bidirectional Reflectance Spectroscopy 5. The Coherent Backscatter Opposition Effect and Anisotropic Scattering. *Icarus*, 157(2):523–534, 2002. 10.1006/icar.2002.6853.

Hapke, B. W., Nelson, R. M., and Smythe, W. D. The opposition effect of the moon: The contribution of coherent backscatter. *Science*, 260(5107):509, 1993.

Helfenstein, P. and Shepard, M. K. Testing the Hapke photometric model: Improved inversion and the porosity correction. *Icarus*, 215(1):83–100, 2011. 10.1016/j.icarus.2011.07.002.

Howell, S. B. *Handbook of CCD astronomy*. Cambridge University Press, Cambridge, 2000.

Kaasalainen, M. and Lamberg, L. Inverse problems of generalized projection operators. *Inverse Problems*, 22(3):749–769, 2006. 10.1088/0266-5611/22/3/002.

REFERENCES

Kaasalainen, M., Lamberg, L., Lumme, K., and Bowell, E. Interpretation of lightcurves of atmosphereless bodies. I - General theory and new inversion schemes. *Astronomy and Astrophysics*, 259(1):318–332, 1992.

Kaasalainen, M., Mottola, S., and Fulchignoni, M. Asteroid Models from Disk-integrated Data. In Bottke, W. F. J., Cellino, A., Paolicchi, P., and Binzel, R., editors, *Asteroids III*. The University of Arizona Press, Tucson, AZ, 2002.

Kaasalainen, M. and Torppa, J. Optimization Methods for Asteroid Lightcurve Inversion I. Shape Determination. *Icarus*, 153(1):24–36, 2001. 10.1006/icar.2001 .6673.

Kaasalainen, M., Torppa, J., and Muinonen, K. Optimization Methods for Asteroid Lightcurve Inversion II. The Complete Inverse Problem. *Icarus*, 153(1):37–51, 2001. 10.1006/icar.2001.6674.

Kohout, T., Čuda, J., Filip, J., Britt, D., Bradley, T., Tuček, J., Skála, R., Kletetschka, G., et al. Space weathering simulations through controlled growth of iron nanoparticles on olivine. *Icarus*, 237:75–83, 2014. 10.1016/j.icarus.2014.04 .004.

Li, J.-Y., Helfenstein, P., Buratti, B. J., Takir, D., and Clark, B. E. Asteroid Photometry. In Michel, P., DeMeo, F. E., and Bottke, W. F., editors, *Asteroids IV*. University of Arizona Press, Tucson, AZ, 2015.

Lumme, K. and Bowell, E. Radiative transfer in the surfaces of atmosphereless bodies. I - Theory. *The Astronomical Journal*, 86:1694, 1981. 10.1086/113054.

Magnusson, P., Barucci, M. A., Drummond, J. D., Lumme, K., Ostro, S. J., Surdej, J., Taylor, R. C., and Zappalà, V. Determination of pole orientations and shapes of asteroids. *Asteroids II*, 1989.

McKay, D., Heiken, G., Basu, A., Blanford, G., Simon, S., Reedy, R., French, B. M., and Papike, J. The Lunar Regolith. In *Lunar Sourcebook*, pages 285–356. Cambridge University Press, Cambridge, 1991.

McKay, D. S., Carter, J. L., Boles, W. W., Allen, C. C., and Allton, J. H. JSC-1: A new lunar regolith simulant. *In Lunar and Planetary Inst. Twenty-Fourth Lunar and Planetary Science Conference*, pages 963–964, 1993.

Merrill, G. P. *A Treatise On Rocks, Rock-weathering And Soils*. The MacMillan Company, New York, 1897.

References

Michikami, T., Nakamura, A. M., Hirata, N., Gaskell, R. W., Nakamura, R., Honda, T., Honda, C., Hiraoka, K., et al. Size-frequency statistics of boulders on global surface of asteroid 25143 Itokawa. *Earth, Planets and Space*, 60(1):13–20, 2008. 10.1186/BF03352757.

Mignard, F., Cellino, A., Muinonen, K., Tanga, P., Delbò, M., Dell'Oro, A., Granvik, M., Hestroffer, D., et al. The Gaia Mission: Expected Applications to Asteroid Science. *Earth, Moon, and Planets*, 101(3-4):97–125, 2008. 10.1007/s11038-007 -9221-z.

Minnaert, M. The reciprocity principle in lunar photometry. *The Astrophysical Journal*, 93:403, 1941. 10.1086/144279.

Muinonen, K. Electromagnetic scattering by two interacting dipoles. In *Proceedings of the 1989 URSI International Symposium on Electromagnetic Theory*, pages 420–430. 1989.

Muinonen, K. *Light scattering by inhomogeneous medioa: Backward enhanceement and reversal of linear polarization*. Ph.D. thesis, University of Helsinki, Helsinki, 1990.

Muinonen, K. and Lumme, K. Disk-integrated brightness of a Lommel-Seeliger scattering ellipsoidal asteroid. *Astronomy & Astrophysics*, 584:A23, 2015. 10.1051/ 0004-6361/201526456.

Muinonen, K., Penttilä, A., and Videen, G. Multiple scattering of light in particulate planetary media. In Kolokolova, L. and Levasseur-Regourd, A.-C., editors, *Polarimetry of Stars and Planetary Systems*, pages 114–129. Cambridge University Press, Cambridge, UK, 2015a.

Muinonen, K. and Wilkman, O. Spherical albedo of a Lommel-Seeliger scattering ellipsoidal asteroid. In Chesley, S., Morbidelli, A., and Jedicke, R., editors, *Proceedings of the International Astronomical Union*. Cambridge University Press, 2016.

Muinonen, K., Wilkman, O., Cellino, A., Wang, X., and Wang, Y. Asteroid lightcurve inversion with Lommel-Seeliger ellipsoids. *Planetary and Space Science*, 118:227—-241, 2015b. 10.1016/j.pss.2015.09.005.

Nakamura, T., Noguchi, T., Tanaka, M., Zolensky, M. E., Kimura, M., Tsuchiyama, A., Nakato, A., Ogami, T., et al. Itokawa dust particles: a direct link be-

tween S-type asteroids and ordinary chondrites. *Science (New York, N.Y.)*, 333(6046):1113–6, 2011. 10.1126/science.1207758.

Näränen, J., Kaasalainen, S., Peltoniemi, J., Heikkilä, S., Granvik, M., and Saarinen, V. Laboratory photometry of planetary regolith analogs. *Astronomy and Astrophysics*, 426(3):1103–1109, 2004. 10.1051/0004-6361:20040556.

Nelson, R. M., Piatek, J. L., Boryta, M. D., Vandervoort, K., Hapke, B. W., Manatt, K. S., Nebedum, A., Shkuratov, Y., et al. Planetary Regolith Analogs Appropriate for Laboratory Measurements. *47th Lunar and Planetary Science Conference*, 2016.

Nicodemus, F., Richmond, J., and Hsia, J. Geometrical considerations and nomenclature for reflectance. *Science And Technology*, 60(October):1–52, 1977. 10.1109/LPT.2009.2020494.

Ostro, S. J. Radar Observations of Asteroid 216 Kleopatra. *Science*, 288(5467):836–839, 2000. 10.1126/science.288.5467.836.

Parviainen, H. and Muinonen, K. Bidirectional reflectance of rough particulate media: Ray-tracing solution. *Journal of Quantitative Spectroscopy & Radiative Transfer*, 110(14-16):1418–1440, 2009.

Peltoniemi, J. I., Hakala, T., Suomalainen, J., Honkavaara, E., Markelin, L., Gritsevich, M., Eskelinen, J., Jaanson, P., and Ikonen, E. Technical notes: A detailed study for the provision of measurement uncertainty and traceability for goniospectrometers. *Journal of Quantitative Spectroscopy and Radiative Transfer*, 146:376–390, 2014. 10.1016/j.jqsrt.2014.04.011.

Racca, G., Marini, A., Stagnaro, L., and van Dooren, J. SMART-1 mission description and development status. *Planetary and Space Science*, 50(14-15):1323–1337, 2002. 10.1016/S0032-0633(02)00123-X.

Russell, H. N. On the light variations of asteroids and satellites. *The Astrophysical Journal*, 24:1, 1906. 10.1086/141361.

Shepard, M. K. and Campbell, B. A. Shadows on a Planetary Surface and Implications for Photometric Roughness. *Icarus*, 134(2):279–291, 1998. 10.1006/icar.1998.5958.

Shepard, M. K. and Helfenstein, P. A test of the Hapke photometric model. *Journal of Geophysical Research*, 112(E3):E03001, 2007. 10.1029/2005JE002625.

REFERENCES

Shkuratov, Y. A Model of Spectral Albedo of Particulate Surfaces: Implications for Optical Properties of the Moon. *Icarus*, 137(2):235–246, 1999. 10.1006/icar.1998.6035.

Shkuratov, Y. G. A diffraction mechanism for the formation of the opposition effect of the brightness of surfaces having a complex structure. *Kinematika i Fizika Nebesnykh Tel (ISSN 0233-7665)*, 4:33–39, 1988.

Stooke, P. J. The surface of asteroid 951 Gaspra. *Earth, Moon and Planets*, 75(1):53–75, 1997. 10.1007/BF00056288.

Suomalainen, J., Hakala, T., Peltoniemi, J., and Puttonen, E. Polarised multiangular reflectance measurements using the finnish geodetic institute field goniospectrometer. *Sensors*, 9(5):3891–3907, 2009. 10.3390/s90503891.

Thomas, P., Joseph, J., Carcich, B., Veverka, J., Clark, B., Bell, J., Byrd, A., Chomko, R., et al. Eros: Shape, Topography, and Slope Processes. *Icarus*, 155(1):18–37, 2002. 10.1006/icar.2001.6755.

Tsuchiyama, A., Uesugi, M., Matsushima, T., Michikami, T., Kadono, T., Nakamura, T., Uesugi, K., Nakano, T., et al. Three-dimensional structure of Hayabusa samples: origin and evolution of Itokawa regolith. *Science (New York, N.Y.)*, 333(6046):1125–8, 2011. 10.1126/science.1207807.

Veverka, J., Robinson, M., Thomas, P., Murchie, S., Bell, J., Izenberg, N., Chapman, C., Harch, A., et al. NEAR at Eros: Imaging and Spectral Results. *Science*, 289(5487):2088–2097, 2000. 10.1126/science.289.5487.2088.

Wilkman, O., Muinonen, K., and Peltoniemi, J. Photometry of dark atmosphereless planetary bodies: an efficient numerical model. *Planetary and Space Science*, 118:250–255, 2015. 10.1016/j.pss.2015.06.004.

Wilkman, O., Muinonen, K., Videen, G., Josset, J.-L., and Souchon, A. Lunar photometric modelling with SMART-1/AMIE imaging data. *Journal of Quantitative Spectroscopy and Radiative Transfer*, 146:529–539, 2014. 10.1016/j.jqsrt.2014.01.015.